Supplementary Information (SI) for ChemComm.
This journal is © The Royal Society of Chemistry 2025

Electronic Supplementary Information (ESI)

Extrinsic Pseudocapacitance of Vanadium Carbide MXene-Poly (3,4-ethylenedioxythiophene) Heterostructure

Suman Yadav and Narendra Kurra*

Department of Chemistry, Indian Institute of Technology Hyderabad, Kandi-502284, Sangareddy, Telangana State, India.

***Corresponding Author**

E-mail: narendra@chy.iith.ac.in

Experimental Section

V_2AlC MAX (particle size, 30 microns) precursor was procured from Y-Carbon, Ukraine Ltd. All chemicals were used as received without further purification.

Synthesis of vanadium carbide (V_2CT_x) MXene:

Typically, MXenes are synthesized from their parent MAX phases using a top-down wet chemical etching route. For the synthesis of vanadium carbide (V_2CT_x) MXene, 1g of vanadium aluminium carbide (V_2AlC) MAX precursor was gradually added to the etchant solution consisting of 8 mL of hydrochloric acid (12 M, Fisher Chemical) and 12 mL of hydrofluoric acid (40 wt%, Hyma).[1] During the etching reaction, fluoride ions selectively etch the aluminium (Al) atomic layer from V_2AlC MAX phase, yielding V_2CT_x MXene. To minimize oxidation and dissolution of the V_2AlC MAX phase during the initial stages, the etching reaction was carried out in an ice bath maintained at 0 °C. Once the hydrogen gas evolution (bubbles formation) ceased, the reaction mixture was transferred to an oil bath at 50 °C, and was constantly stirred for 80 h at 400 rpm. Upon completion of the etching reaction, the resulting acidic V_2CT_x MXene dispersion was repeatedly washed with deionized (DI) water via centrifugation at 3500 rpm for 5 min each time. A green-coloured supernatant obtained after the first wash was discarded and repeatedly washed until the pH reached ~6-7. The resulting V_2CT_x MXene was dispersed in DI water and filtered through a Celgard membrane (pore size, 60 nm) using a vacuum-assisted filtration setup and further vacuum dried at 80 °C for 12 h.

Fabrication of poly (3,4-ethylenedioxythiophene)/vanadium carbide heterostructure electrodes:

To fabricate the heterostructured poly (3,4-ethylenedioxythiophene)/vanadium carbide (PEDOT/V_2CT_x) electrodes, firstly, a thick slurry was prepared by thoroughly mixing vacuum-dried V_2CT_x MXene (80 wt%), carbon black (10 wt%, Super P C45, Timical), and polyvinylidene fluoride (PVDF) binder (10 wt%, Sigma–Aldrich) using mortar and pestle. N-methyl-2-pyrrolidine (NMP) was gradually added dropwise during grinding, resulting in a uniform thick slurry. The slurry was uniformly cast onto a graphite foil current collector using a doctor blade coater and vacuum-dried at 80 °C for 12 h. Furthermore, electrochemical polymerization of poly(3,4-ethylenedioxythiophene) (PEDOT) was carried out in a standard three-electrode glass cell containing 100 µL of 3,4-ethylenedioxythiophene (EDOT, 97%, Sigma Aldrich) dissolved in 15 mL of 60 mM calcium bis(trifluoromethanesulphonyl)imide

[$Ca(TFSI)_2$] and 30 mM lithium bis(trifluoromethanesulphonyl)imide (LiTFSI) in acetonitrile electrolyte. The vacuum-dried V_2CT_x MXene coated on a graphite foil was immersed in the electrolytic bath as the working electrode, Ag wire as the reference electrode, and graphite rod as the counter electrode. A constant anodic potential of 1.2 V was applied using a BioLogic SP-150e workstation (BioLogic, France), and a total of 2.24 C of charge was passed during the electrochemical polymerization of PEDOT on V_2CT_x MXene. The resulting PEDOT/V_2CT_x heterostructure electrodes were thoroughly washed with acetonitrile to remove residual EDOT and electrolyte salts, followed by vacuum drying at 60 °C for 6 h.

Fabrication of the activated carbon (AC) films:

Activated carbon (AC, YP50F grade) films were fabricated by blending 95 wt% YP50F (Kuraray, Japan) with 5 wt% polytetrafluoroethylene (PTFE, 60 wt% dispersion in water, Sigma Aldrich). The components were thoroughly ground using a mortar and pestle, and a small amount of ethanol was added to form a uniform paste. The resulting paste was rolled into films of approximately 100 µm thickness and subsequently dried in a vacuum oven at 70 °C overnight. The dried AC films were then punched into 3 mm diameter discs and employed as counter electrodes for electrochemical measurements.

Material Characterization:

The XRD patterns of V_2AlC MAX, V_2CT_x MXene, and PEDOT/V_2CT_x heterostructure were recorded using a powder X-ray diffractometer (Malvern PANalytical, UK) equipped with a CuK_α (wavelength, 1.5406 Å) radiation source. For each pattern, the step size and dwell time were 0.012° and 0.13 s, respectively. The nature of chemical bonding and the fingerprint region of V_2CT_x MXene was investigated using infrared spectroscopy, and spectrum was recorded in a Jasco FT-IR spectrometer in the range of 400 - 4000 cm^{-1} using a KBr pellet. The morphology of PEDOT and the PEDOT/V_2CT_x heterostructure electrode was imaged using field emission scanning electron microscopy (FESEM) (JEOL JIB4700F). Raman spectra were recorded for PEDOT and PEDOT/V_2CT_x heterostructure electrode using a WITec confocal Raman microscope (alpha 300R series) with an excitation wavelength of 532 nm, and 10% laser power. Each spectrum was recorded with three accumulations and an integration time of 30 s with a grating size of 600 g/mm.

Electrochemical measurements:

Electrochemical analyses, including cyclic voltammetry (CV), galvanostatic charge-discharge (GCD), and electrochemical impedance spectroscopy (EIS), were carried out using an SP-150e electrochemical workstation (BioLogic, France). All measurements were conducted at room temperature in a three-electrode Swagelok cell configuration, employing V_2CT_x MXene and PEDOT/V_2CT_x heterostructure as the working electrode, activated carbon as the counter electrode, and Ag/AgCl as the reference electrode. Glass microfiber membranes (Whatman) were used as separators, which hold the electrolyte. The electrochemical behavior of V_2CT_x MXene, and PEDOT/V_2CT_x heterostructure electrodes was investigated in 1M calcium bis(trifluoromethanesulphonyl)imide [$Ca(TFSI)_2$] (TCI) aqueous electrolyte. Cyclic voltammograms for all electrodes were collected at scan rates of 2, 5, 10, 20, 50, and 100 mV s^{-1}, while GCD profiles were recorded at various current densities.

Specific capacity was estimated by integrating current versus time plots.

$$Specific\ capacity = \frac{1}{m}\int i dt \tag{1}$$

The gravimetric capacitance (C_g) was calculated from the CV scan curve based on the following expression

$$C_g(\mathrm{F\ g^{-1}}) = \frac{1}{Vmv}\int_{V1}^{V2} i\, dV \tag{2}$$

where i is the current (mA), V is the potential window (V_2 - V_1) of the CV scan, v stands for the scan rate (mV s^{-1}), dV is infinitesimal changes in potential, and m is the mass of the active material (mg) on the working electrode.

The real capacitance, $C^{'}$ and imaginary capacitance, $C^{''}$ were calculated according to the following equations:

$$C^{'} = -Z^{''}/2\pi f|Z|^2 \tag{3}$$

$$C^{''} = Z^{'}/2\pi f|Z|^2 \tag{4}$$

where |Z| is the absolute value of impedance (Ω), Z′ and Z″ are the real and imaginary components of impedance, respectively, and f is the frequency (Hz).

The charge transfer and mass transfer kinetics across electrode|electrolyte interfaces were investigated by employing staircase potentio-electrochemical impedance spectroscopy (SPEIS). In this technique, impedance measurements were made by holding the working electrode at different DC applied potentials while imposing a small sinusoidal voltage of 10 mV. SPEIS measurements were done by applying step potential intervals of 50 mV DC potential with an AC amplitude of 10 mV to V_2CT_x MXene and PEDOT/V_2CT_x heterostructure electrodes in the frequency range of 100 kHz - 10 mHz.

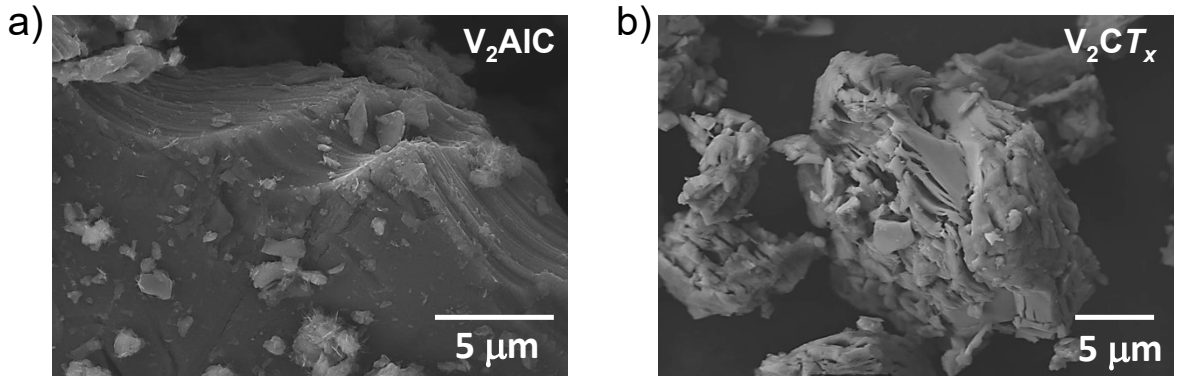

Fig. S1: Field emission scanning electron microscopy (FESEM) images of (a) V_2AlC MAX and (b) V_2CT_x MXene.

The morphological transformation from dense and compact V_2AlC MAX phase to a characteristic accordion-like V_2CT_x MXene shows the removal of the Al atomic layer during the etching process (Fig. S1).

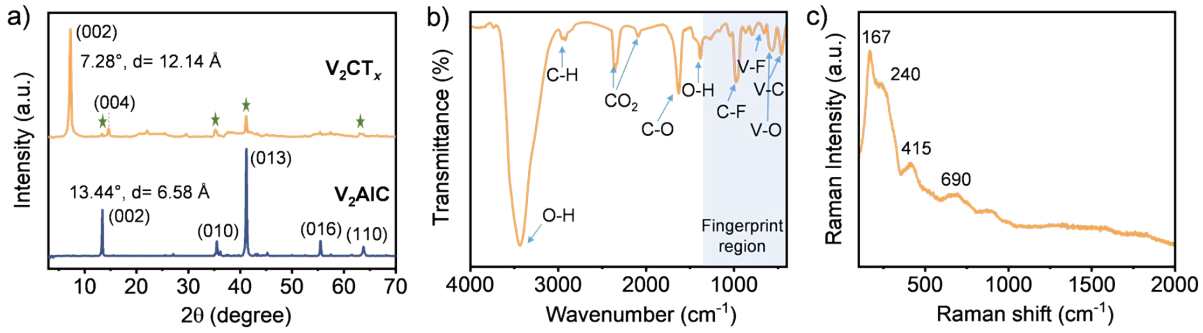

Fig. S2: (a) X-ray diffraction patterns of V_2AlC MAX phase and V_2CT_x MXene, where peaks marked with (★) correspond to V_2AlC MAX precursor. (b) Fourier transform infrared (FTIR) spectrum of V_2CT_x MXene recorded in a range of 400 - 4000 cm^{-1}. (c) Raman spectrum of V_2CT_x MXene.

The increase in *d*-spacing after the removal of Al atomic layer from V_2AlC MAX precursor is evident from Fig. S2a. The decrease in the characteristic (002) peak of V_2CT_x from 2θ of 13.44° to 7.28°, with a corresponding increase in the *d*-spacing of 5.56 Å. Fig. S2b shows the FT-IR

spectrum of V_2CT_x MXene exhibiting confined water and fingerprint region. The absorption band appear between 3200 to 3600 cm^{-1} corresponds to the O-H stretching vibration and the peak at 1378 cm^{-1} corresponds to surface terminated -OH group. Additionally, the peaks at 1629, 974, and 571 cm^{-1} corresponds to the stretching vibrations of C-O, C-F, and V-O bond respectively. The characteristic peak appear at 458 cm^{-1} in fingerprint region is due to V-C bond of V_2CT_x MXene. Fig. S2c shows the Raman spectrum of V_2CT_x MXene exhibiting four broad peaks (two out-of-plane vibrations and two in-plane vibrations). The peaks located in the low-frequency region at around 167 cm^{-1} and 240 cm^{-1} correspond to in-plane and out-of-plane (A_{1g} symmetric) transition metal atom vibrations, respectively. A broad peak at 415 cm^{-1} corresponds to the surface terminations of V_2CT_x MXene and arises from collective vibrations of atoms within the monolayer structure. The peak at 690 cm^{-1} is due to A_{1g} asymmetric vibrations.

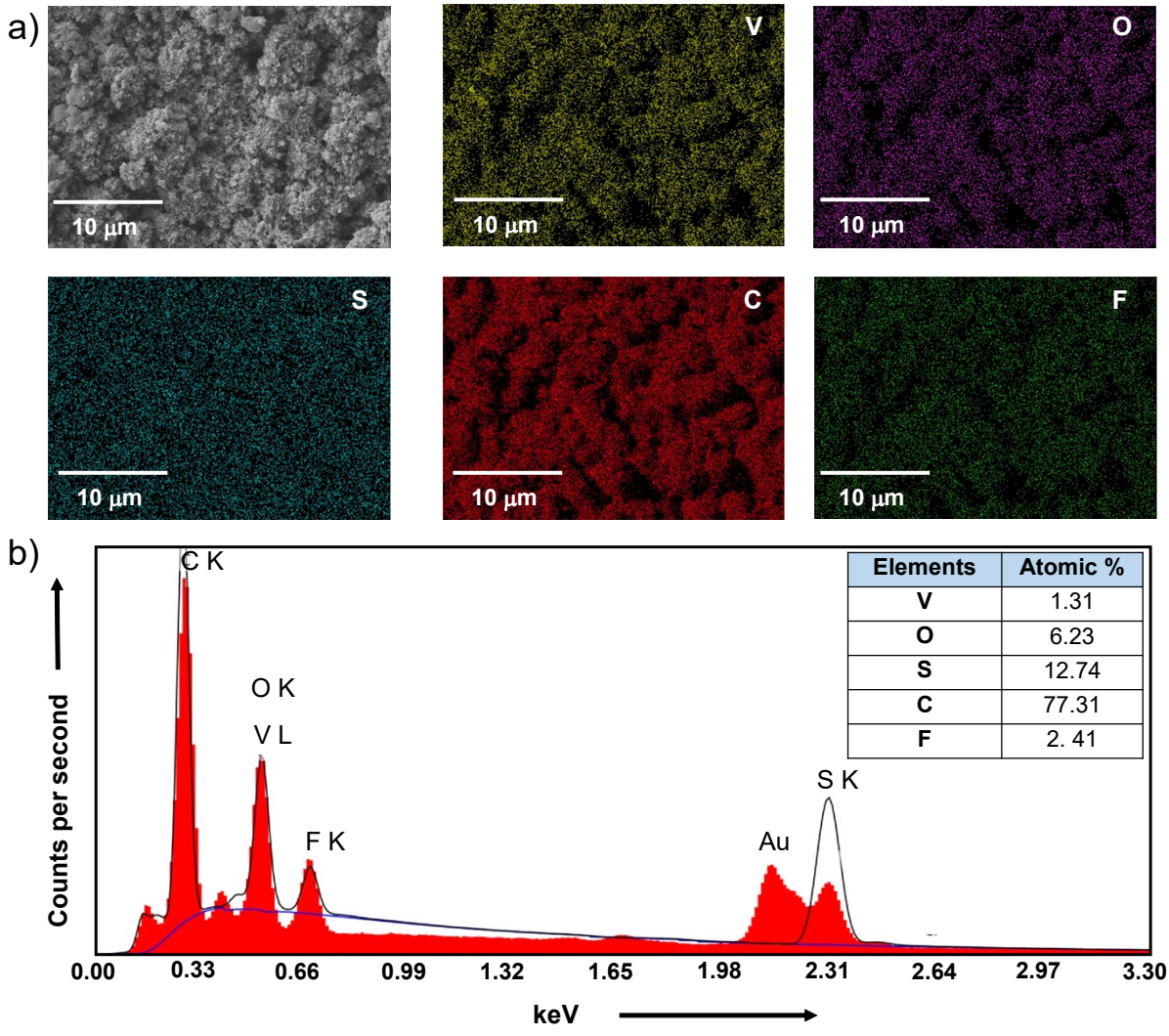

Fig. S3: (a) Scanning electron microscopy (SEM) image of PEDOT/V_2CT_x heterostructure electrode and corresponding elemental-mapping images (V, O, S, C, and F elements). (b) Energy dispersive X-ray (EDX) analysis of PEDOT/V_2CT_x heterostructure electrode with atomic percentage of V, O, S, C, and F elements. However, due to low resolution of EDS data, it is difficult to quantify in an absolute manner. Therefore, relative compositional analysis is provided from the following EDS spectrum

The SEM images of PEDOT/ V_2CT_x heterostructure electrode and the elemental analysis confirm the uniform distribution of V, C, and S elements across the V_2CT_x MXene surface, indicating a homogeneous coating of PEDOT on the pristine V_2CT_x MXene electrode.

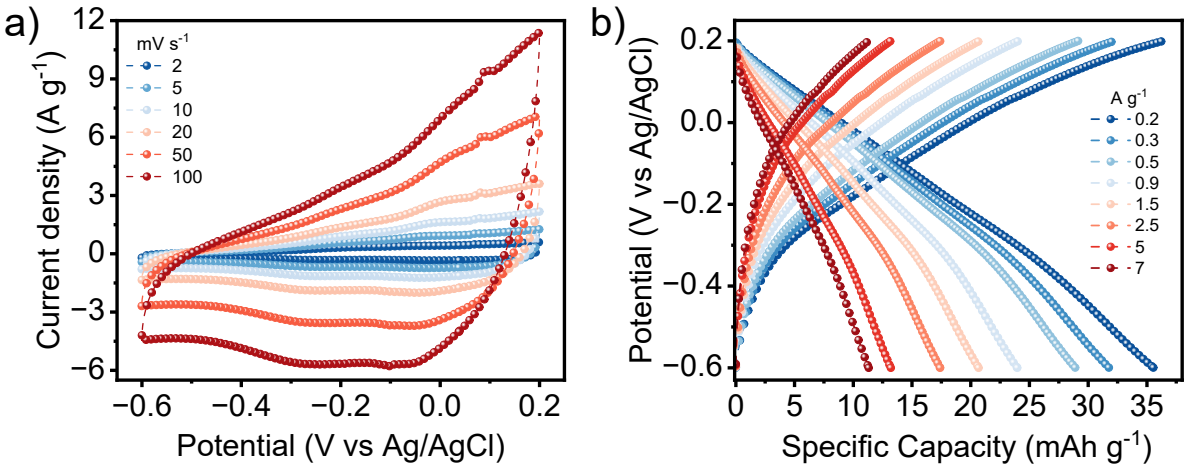

Fig. S4: Electrochemical performance of pristine V_2CT_x MXene in 1M $Ca(TFSI)_2$ aqueous electrolyte. (a) Cyclic voltammograms (CVs) at various scan rates and (b) Galvanostatic charge-discharge (GCD) profiles at different current densities.

The pristine V_2CT_x MXene shows cyclic voltammograms with an anodic potential limit of 0.2 V (vs Ag/AgCl). The typical calciation capacity of V_2CT_x MXene was found to be 36 mAh g^{-1} at a current density of 0.2 A g^{-1} in 1M $Ca(TFSI)_2$ aqueous electrolyte and retained 12 mAh g^{-1} even at high current density of 7 A g^{-1}.

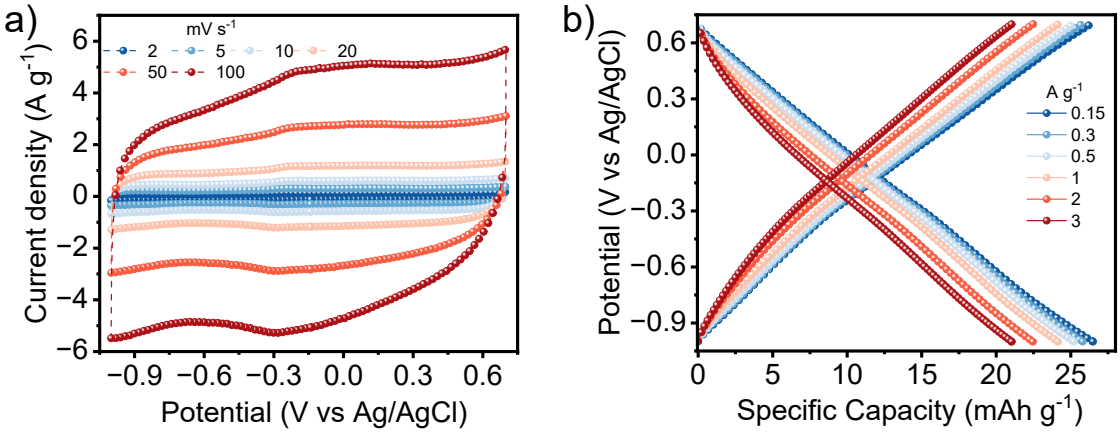

Fig. S5: (a) Cyclic voltammograms (CVs) of PEDOT in 1M $Ca(TFSI)_2$ aqueous electrolyte at various scan rates and (b) Galvanostatic charge-discharge (GCD) profiles of PEDOT in 1M $Ca(TFSI)_2$ aqueous electrolyte at different current densities.

The PEDOT electrode exhibits quasi-rectangular-type cyclic voltammograms within an operation potential window of -1 to 0.7 V vs Ag/AgCl. The typical calciation capacity of PEDOT was found to be 27 mAh g^{-1} at a current density of 0.15 A g^{-1} in 1M $Ca(TFSI)_2$ aqueous electrolyte and retained 21 mAh g^{-1} even at a high current density of 3 A g^{-1}.

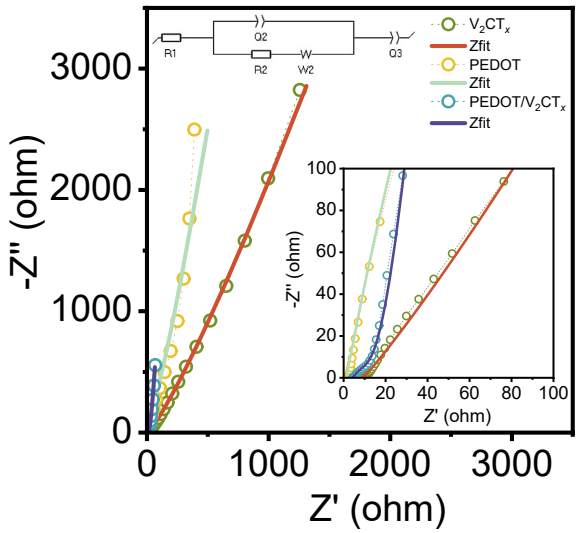

Fig. S6: Electrochemical impedance spectra (EIS) of V_2CT_x MXene, PEDOT, and PEDOT/ V_2CT_x heterostructure electrode in 1M $Ca(TFSI)_2$ aqueous electrolyte at open circuit voltage and the high frequency regime spectra shown in the inset.

The charge transfer kinetics of V_2CT_x MXene, PEDOT, and PEDOT/V_2CT_x heterostructure electrodes in 1M $Ca(TFSI)_2$ aqueous electrolyte were examined using electrochemical impedance spectroscopy (EIS) over a frequency range from 100 kHz to 10 mHz. The X-axis intercept in the high-frequency regime is the equivalent series resistance (ESR), which is found to be 9.2, 1.4, and 4.3 Ω for V_2CT_x MXene, PEDOT, and PEDOT/V_2CT_x heterostructure electrodes, respectively. The ESR value of PEDOT/V_2CT_x heterostructure is lower than that of pristine V_2CT_x MXene, indicates that the conductive PEDOT coating effectively reduces the electrode resistance, besides the ease of ion transport. However, PEDOT/V_2CT_x heterostructure exhibits close to 90º profile in the low frequency region, indicating a predominantly capacitive type response.

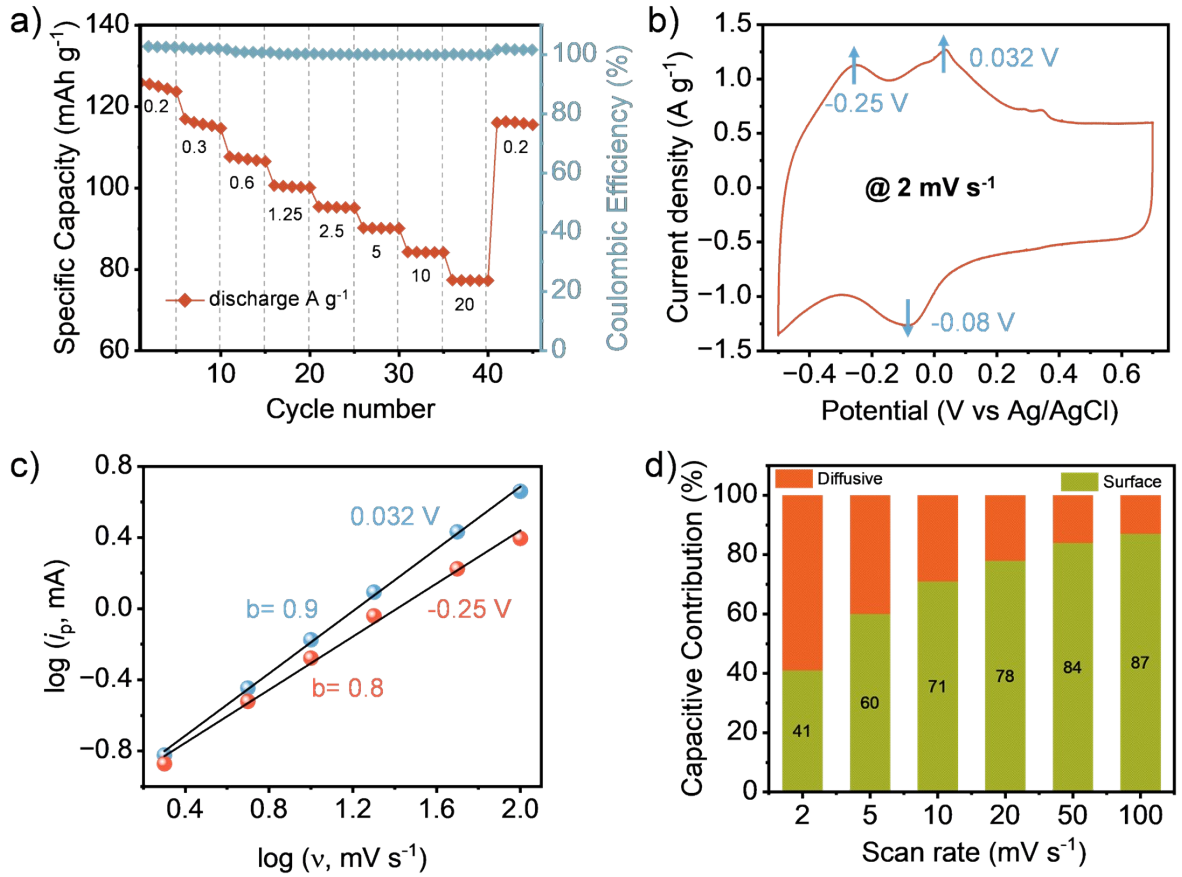

Fig. S7: (a) Rate performance of PEDOT/V_2CT_x heterostructure electrode in 1 M $Ca(TFSI)_2$ aqueous electrolyte. (b) Cyclic voltammogram (CV) of PEDOT/V_2CT_x heterostructure in 1M $Ca(TFSI)_2$ aqueous electrolyte at a scan rate of 2 mV s^{-1}. (c) *log* (peak current) vs *log* (scan rate) plot estimated at anodic potentials of 0.032 V and -0.25 V vs Ag/AgCl. (d) Surface and diffusion-controlled contributions to current response at various scan rates.

The rate capability of PEDOT/V_2CT_x electrode over various current densities ranging from 0.2 to 20 A g^{-1} is shown in Fig. S7a. The electrode exhibited a calciation capacity of 125 mAh g^{-1} at a current density of 0.2 A g^{-1} with a Coulombic efficiency of 100%. At higher current density of 20 A g^{-1}, 62% capacity retention (77 mAh g^{-1}) was observed, signifying the good rate capability of the PEDOT/V_2CT_x heterostructure electrode. Fig. S7b shows the cyclic voltammograms of PEDOT/V_2CT_x heterostructure at a scan rate of 2 mV s^{-1}, highlighting pair of anodic and a broad cathodic peak. The PEDOT/V_2CT_x heterostructure showed a hybrid type of charge transfer kinetics with *b*-values of 0.9 and 0.8 at anodic potential of -0.25 and 0.035 V vs Ag/AgCl (Fig. S7c). Further, the capacitive and diffusive contributions of PEDOT/V_2CT_x heterostructure electrode at different scan rates is shown in Fig. S7d. At a scan rate of 2 mV s^{-1}, the capacitive contribution is 41%, which increases to 87% at 100 mV s^{-1}.

Table S1: Electrochemical performance of V_2CT_x MXene reported in various aqueous electrolytes.

S. No.	Electrode	Electrolyte	Potential window	Specific Capacitance ($F\ g^{-1}$)	Number of cycles	References
1.	V_2CT_x	1 M H_2SO_4	-0.5 to 0.1 V vs SCE	665	1000	2
2.		1 M KOH	-1.2 to -0.6 V vs SCE	382	1000	
3.		1 M Li_2SO_4	-1.1 to 0.1 V vs SCE	338	1000	
4.	V_2CT_x	0.5 M Li_2SO_4	-1.2 to 0.0 V vs Ag wire	208	1000	3
5.		1 M $MgSO_4$	-1.2 to 0.0 V vs Ag wire	225	1000	
6.		1 M Na_2SO_4	-1 to -0.2 V vs Ag wire	120	1000	
7.		0.5 M K_2SO_4	-1 to -0.2 V vs Ag wire	104	1000	
8.	Li-V_2CT_x	1 M LiOH	-1.4 to -0.8 V vs Ag/AgCl	386	-	4
9.	V_2CT_x	2 M $ZnSO_4$	-1 to 0.2 V vs Ag/AgCl	481	60000	5
10.	**PEDOT/V_2CT_x**	**1 M $Ca(TFSI)_2$**	**-0.5 to 0.7 V vs Ag/AgCl**	**322**	**1000**	**This work**

Abbreviation-

V_2CT_x- Vanadium carbide MXene, H_2SO_4- sulphuric acid, KOH- Potassium hydroxide, Li_2SO_4- Lithium sulphate, $MgSO_4$- Magnesium sulphate, Na_2SO_4- sodium sulphate, K_2SO_4- Potassium sulphate, LiOH- Lithium hydroxide, $ZnSO_4$- Zinc sulphate, $Ca(TFSI)_2$- Calcium bis(trifluoromethanesulphonyl)imide.

Table S2: Electrochemical performance of reported electrode materials for Ca-ion storage.

S. No.	Electrode	Electrolyte	Potential window	Specific Capacity (mA h g^{-1})	Cycle number	References
1.	CuHCF	2.5 m $Ca(NO_3)_2$/ H_2O	0.4 to 1.0 V vs Ag/AgCl	55 @ 1C	2000	6
2.	PNDIE	2.5 m $Ca(NO_3)_2$/ H_2O	-0.9 to 0.2 V vs Ag/AgCl	143 @ 2C	4000	6
3.	PTCDI	1 m $CaCl_2 \cdot 2H_2O$/ H_2O	-1.0 to 0.2 V vs Ag/AgCl	100 @ 0.5 A g^{-1}	1000	7
4.	PT	1 M $CaCl_2$ / H_2O	-1.0 to 0.6 V vs Ag/AgCl	150 @ 5 A g^{-1}	3000	8
5.	PANI	2.5 M $Ca(NO_3)_2$/ H_2O	-0.6 to 0.4 V vs Ag/AgCl	120 @ 0.15 A g^{-1}	200	9
6.	PTCDI	1.5 M $Ca(ClO_4)_2$/ PC	-1.6 to 0.8 V vs ACS25	100 @ 0.2 A g^{-1}	1000	10
7.	V_2CT_x:NiHCF	5 M $Ca(TFSI)_2$/ H_2O	-1 to 0.7 V vs Ag/AgCl	140 @ 0.5 A g^{-1}	1000	11
8.	V_2CT_x	5 M $Ca(TFSI)_2$/ H_2O	-0.6 to 0.7 V vs Ag/AgCl	88 @ 0.5 A g^{-1}	10000	12
9.	$CaV_6O_{16} \cdot 2.8H_2O$	0.3 M $Ca(TFSI)_2$	-1.3 to 0.8 V vs ACC	175 @ 0.05 A g^{-1}	1000	13
10.	N_1VPF_3	0.5 m $Ca(PF_6)_2$ EC/PC/EMC/DMC	-1 to 1.5 V vs AC	110 @ 0.01 A g^{-1}	2000	14
11.	FeS_2	0.5 M $Ca(BH_4)_2$ + 1.5 M $LiBH_4$/THF	0.9 to 2.2 V vs Ca/Ca^{2+}	493 @ C/8	200	15

12.	CVO	1 M $Ca(ClO_4)_2$ / AN: H_2O (4:1)	0.0 to 1.2 V vs Ag/AgCl	158 @ 0.2 A g^{-1}	2000	16
13.	$NaV_2(PO_4)_3$	1 M $Ca(TFSI)_2$/AN	-0.4 – 0.4 V vs AC	81 @ 35 mA g^{-1}	-	17
14.	TiS_2	0.1 M $Ca(OTf)_2$/ PC/DMC	1.5 – 3 V	90 @ 0.05 A g^{-1}	-	18
15.	Graphite	1 M $Ca(TFSI)_2$/ Tetraglyme	-2.7 – 0.7 V vs SHE	64 @ 0.5 A g^{-1}	-	19
16.	**PEDOT/V_2CT_x**	**1M $Ca(TFSI)_2$/ H_2O**	**-0.5 to 0.7 V vs Ag/AgCl**	**125 @** 0.2 A g^{-1}	**1000**	**This work**

Abbreviation-

CuHCF- copper hexacyanoferrate, PNDIE- poly[*N*,*N*′-(ethane-1,2-diyl)-1,4,5,8-naphthalenetetracarboxiimide], PTCDI- perylene tetra-carboxylicdiimide, PT- 5,7,12,14-pentacenetetrone, PANI- polyaniline, V_2CT_x- Vanadium carbide MXene, NiHCF- nickel hexacyanoferrate, N_1VPF_3- Na-vacant $Na_1V_2(PO_4)_2F_3$, FeS_2- Iron disulfide, CVO- $Ca_{0.25}V_2O_5 \cdot 1.1H_2O$, TiS_2- Titanium disulfide, PEDOT- poly(3,4-ethylenedioxythiophene, $Ca(NO_3)_2$- calcium nitrate, $CaCl_2$- calcium chloride, $Ca(ClO_4)_2$- calcium perchlorate, $Ca(TFSI)_2$- calcium bis(trifluoromethanesulphonyl)imide, $Ca(PF_6)_2$- calcium hexafluorohospate, EC- ethylene carbonate, PC- propylene carbonate, EMC- ethyl methyl carbonate, DMC- dimethyl carbonate, $Ca(BH_4)_2$- calcium borohydride, $LiBH_4$- lithium borohydride, THF- tetrahydrofuran, AN- acetonitrile, $Ca(OTf)_2$- calcium trifluoromethanesulfonate.

References

1. K. Matthews, T. Zhang, C. E. Shuck, A. VahidMohammadi and Y. Gogotsi, *Chem. Mater.*, 2022, **34**, 499-509.
2. Y. Song, L. Hu and Y. Xin, *J. Electrochem. Soc.*, 2022, **169**, 072510.
3. C. Chen, D. Pang, X. Wang, G. Chen, F. Du and Y. Gao, *Chin. Phys. Lett.*, 2021, **38**, 058201.
4. T. Zhang, K. Matthews, A. VahidMohammadi, M. Han and Y. Gogotsi, *ACS Energy Lett.*, 2022, **7**, 3864-3870.
5. W. Chen, L. Zhang, H. Ren, T. Miao, Z. Wang, K. Zhan, J. Yang and B. Zhao, *J. Colloid Interface Sci.*, 2022, **626**, 59-67.
6. S. Gheytani, Y. Liang, F. Wu, Y. Jing, H. Dong, K. K. Rao, X. Chi, F. Fang and Y. Yao, *Adv. Sci.*, 2017, **4**, 1700465.
7. R. Li, J. Yu, F. Chen, Y. Su, K. C. Chan and Z.-L. Xu, *Adv. Funct. Mater.*, 2023, **33**, 2214304.

8. C. Han, H. Li, Y. Li, J. Zhu and C. Zhi, *Nat. Commun.*, 2021, **12**, 2400.
9. M. Adil, A. Sarkar, A. Roy, M. R. Panda, A. Nagendra and S. Mitra, *ACS Appl. Mater. Interfaces*, 2020, **12**, 11489-11503.
10. W.-Y. Jao, C.-W. Tai, C.-C. Chang and C.-C. Hu, *Energy Storage Mater.*, 2023, **63**, 102990.
11. S. Yadav, D. Michael and N. Kurra, *ACS Appl. Mater. Interfaces*, 2025, **17**, 57124-57132.
12. S. Yadav and N. Kurra, *Small*, 2025, **21**, 2503657.
13. J. Wang, J. Wang, Y. Jiang, F. Xiong, S. Tan, F. Qiao, J. Chen, Q. An and L. Mai, *Adv. Funct. Mater.*, 2022, **32**, 2113030.
14. C. Chen, F. Shi, S. Zhang, Y. Su and Z.-L. Xu, *Small*, 2022, **18**, 2107853.
15. Z. Meng, A. Reupert, Y. Tang, Z. Li, G. Karkera, L. Wang, A. Roy, T. Diemant, M. Fichtner and Z. Zhao-Karger, *ACS Appl. Mater. Interfaces*, 2022, **14**, 54616-54622.
16. X. Qin, X. Zhao, G. Zhang, Z. Wei, L. Li, X. Wang, C. Zhi, H. Li, C. Han and B. Li, *ACS Nano*, 2023, **17**, 12040-12051.
17. S. Kim, L. Yin, M. H. Lee, P. Parajuli, L. Blanc, T. T. Fister, H. Park, B. J. Kwon, B. J. Ingram, P. Zapol, R. F. Klie, K. Kang, L. F. Nazar, S. H. Lapidus and J. T. Vaughey, *ACS Energy Lett.*, 2020, **5**, 3203-3211.
18. C. Lee, Y.-T. Jeong, P. M. Nogales, H.-Y. Song, Y. Kim, R.-Z. Yin and S.-K. Jeong, *Electrochem. Commun.*, 2019, **98**, 115-118.
19. S. J. Richard Prabakar, A. B. Ikhe, W. B. Park, K.-C. Chung, H. Park, K.-J. Kim, D. Ahn, J. S. Kwak, K.-S. Sohn and M. Pyo, *Adv. Sci.*, 2019, **6**, 1902129.